



Efficient prediction of thermal history in wire and arc additive manufacturing combining machine learning and numerical simulation

Van Thao Le¹ · Manh Cuong Bui² · Think Quy Duc Pham^{3,4} · Hoang Son Tran⁵ · Xuan Van Tran³

Received: 4 October 2022 / Accepted: 19 April 2023 / Published online: 24 April 2023
© The Author(s), under exclusive licence to Springer-Verlag London Ltd., part of Springer Nature 2023

Abstract

Among metallic additive manufacturing technologies, wire and arc additive manufacturing (WAAM) has been recently adopted to manufacture large industrial components. In this process, controlling the temperature evolution is very important since it directly influences the quality of the deposited parts. Typically, the temperature history in WAAM can be obtained through experiments and/or numerical simulations, which are generally time-consuming and expensive. In this research, we developed a robust surrogate model (SM) for predicting the temperature history in WAAM based on the combination of machining learning (ML) and finite element (FE) simulation. The SM model was built to predict the temperature history in the WAAM of single weld tracks. For this purpose, the FE model was first developed and validated against experiments. The FE model was subsequently used to generate the data to train ML models based on feed-forward neural network (FFNN). The trained SM model can fast and accurately predict the temperature history in the cases which were not previously used for training with a very high accuracy of more than 99% and in a very short time with only 38 s (after being trained) as compared with 5 h for a FE model. The trained SM can be used for studies that require a large number of simulations such as uncertainty quantification or process optimization.

Keywords Wire and arc additive manufacturing (WAAM) · Surrogate model · Finite element simulation · Machine learning · Thermal history · 316L

1 Introduction

Being considered an advanced method of manufacturing products by adding materials layer-by-layer, additive manufacturing (AM) technologies can fabricate very complex components [1]. Especially, metal AM (MAM) has been

increasingly used in important industrial sectors such as aeronautics, automobile, shipbuilding, and tooling [2–4]. Together with powder-bed-fusion (PBF) AM technologies, directed energy deposition (DED) is an important technique in the MAM group [5]. DED can use either a laser or an arc source to melt metallic powder/wire and to directly deposit into a part layer-by-layer through a nozzle [6, 7]. A common multi-axis CNC machine or a robot can perform the shaping motion in DED. Therefore, DED technologies are commonly used to fabricate components with medium to large dimensions compared to PBF-AM [6].

Among DED technologies, the process using metallic wire and an arc as the energy source, also called WAAM [8], allows the highest rate of material deposition [9, 10], so quite suitable to fabricate large components. WAAM systems also require a lower investment cost compared to other powder-based MAM systems because they can be built using available welding equipment and mechanisms such as machine tools and robots [11–14]. In addition, the metal wires available in the welding market with relatively low costs can be used in WAAM. The use of

✉ Xuan Van Tran
xuantv@tdmu.edu.vn

¹ Advanced Technology Center, Le Quy Don Technical University, Hanoi, Vietnam

² Faculty of Mechanical Engineering, Le Quy Don Technical University, Hanoi, Vietnam

³ Institute of Southeast Vietnamese Studies (ISVS), Thu Dau Mot University, Thu Dau Mot, Binh Duong, Vietnam

⁴ Urban and Environmental Engineering, Materials and Solid Mechanics, University of Liège, Quartier Polytech 1, Allée de La Découverte 9 (B52), B-4000 Liège, Belgium

⁵ Departement Metal Production & Recycling/Iron & Steelmaking, CRMGroup - CRM Sart Tilman (Centre de Recherches Métallurgiques), Liège, Belgium

the metal wire is also safer for operators and the environment compared to that of metal powder [15]. These advantages and benefits of WAAM make it become one of the most competitive technologies for fabricating components with large dimensions and low production costs, especially for industrial applications. In fact, researchers and industrial manufacturers have recently focused on WAAM [16].

One of the main challenges in WAAM processes is the accumulation of the heat during the printing process [9]. As the number of deposited layers increases, the accumulated heat significantly increases, leading to the slag of melted material, thermal distortion, and residual stress. It also greatly influences the solid state transformation of the deposited material [17–20]. Moreover, it is largely accepted that the microstructures of parts fabricated by WAAM are strongly dependent of the thermal history [21]. Many authors investigated the thermal history and its influences on microstructures, mechanical characteristics, thermal distortion, and residual stress (Cunningham et al. 2018). For example, Zhao et al. [18] investigated the thermal behavior during the WAAM process of thin walls via experiment and simulation. They found that the melt pool temperature gradient and the rate of cooling decreased with an increase of the deposition height. This was due to the heat accumulation during the layer deposition. Similarly, using a thermal infrared camera, Yang et al. [22] observed that the high area temperature behind the melt pool was gradually more significant with the deposition height. Moreover, the interlayer cooling time could enhance the forming quality of as-fabricated thin-wall components. Rodrigues et al. [23] also utilized a thermal infrared camera to study the influence of the thermal cycles on microstructures and characteristics of high-strength-low-alloy (HSLA) steels deposited by WAAM. The authors also observed that the temperature gradient mitigated with the increase in the deposition height. Moreover, as the heat input increased the cooling rate decreased, whereas the solidification time increased. Due to the variation of thermal cycles along the building direction, the microstructure was changed, especially in terms of grain size. Recently, Le et al. [24, 25] analyzed the effects of process parameters and the thermal history on the quality of stainless steel parts made by WAAM via experiment and simulation methods. The authors also reported that the thermal cycles played an important role in the formation and evolution in microstructures and grains' size of the as-fabricated material. Moreover, increasing the travel speed of the weld torch resulted in a refinement in microstructures, thus enhancing the mechanical strengths.

Although the experiment or a combination of experiment and simulation was successfully applied to analyze

the effects of process variables and thermal cycles on characteristics of the WAAM fabricated components, they are generally time-consuming and expensive. The number of experimental tests and simulations was also limited; meanwhile, a large number of combined process variables need to be examined to build a complete process map for predicting the process parameters and product qualities [26]. Recently, machine learning (ML) shows the potential applications to accelerate thermal prediction in MAM by exploiting datasets obtained from experiments and experimentally validated simulations. ML concentrates on algorithms of data modeling and label predictions with the goal of generating robust predictions for the tasks of regression and classification [27]. Modern deep learning (DL) methods have shown great benefits in different sectors from material and product design to manufacturing processes [28].

Taking the advantages of ML and DL, several authors have successfully developed surrogate models (SMs) to predict the thermal evolution in AM robustly. Pham et al. [29] and Fetni et al. [30] proposed SMs for predicting the thermal field in the powder-DED process, where FFNN (feed-forward-neural network) models were adopted. The authors stated that the model accuracy was attained above 99% with a short prediction time. Zhu et al. [28] developed the PINN (physics-informed neural network) codes to predict the melt pool fluid dynamics and temperature in MAM. Roy and Wodo [31] developed a SM based on ANN to predict the thermal field in the fused-filament-fabrication (FFF) process. The authors utilized the data obtained from numerical simulations to train and validate the SM. They showed that the SM could predict the temperature evolution rapidly with high accuracy.

To the best of the authors' knowledge, SMs for the thermal prediction in WAAM are still limited in the literature. Inspired from previous publications [29–32], we developed a SM to predict the temperature variation at any point of the part fabricated by WAAM. The FFNN model was chosen because it has a simple architecture and fast training compared to other complex deep learning models, such as RNN and PINN. In this paper, we focus on the thermal experiment and simulation of the WAAM process of single weld tracks. This step aims to calibrate the thermal simulation model of the WAAM process accurately. In future works, we will extend the applications of this method for the single-track multi-layer or multi-track multi-layer deposition.

The article was structured as follows. In Section 2, the materials and research methodology were presented. In particular, the methodology was described step-by-step. Section 3 is intended for the results and discussion. Lastly, the main findings and conclusions of this research were presented in Section 4.

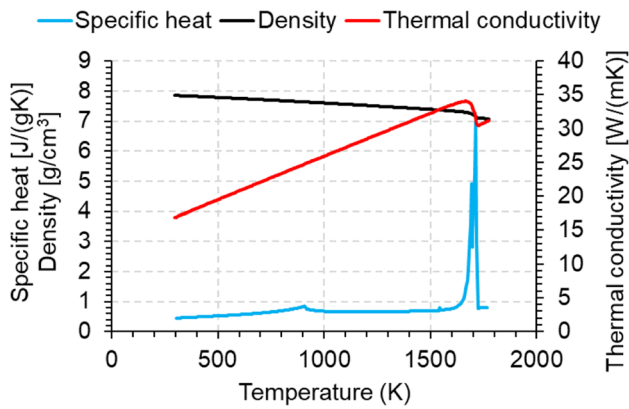


Fig. 1 The density, specific heat, and thermal conductivity of 316L stainless steel as functions of temperatures

2 Materials and methodology

2.1 Materials

In this paper, we focused on the thermal evolution during a single weld track in the WAAM process. The single weld track was fabricated on a 200 mm × 80 mm × 10 mm plate

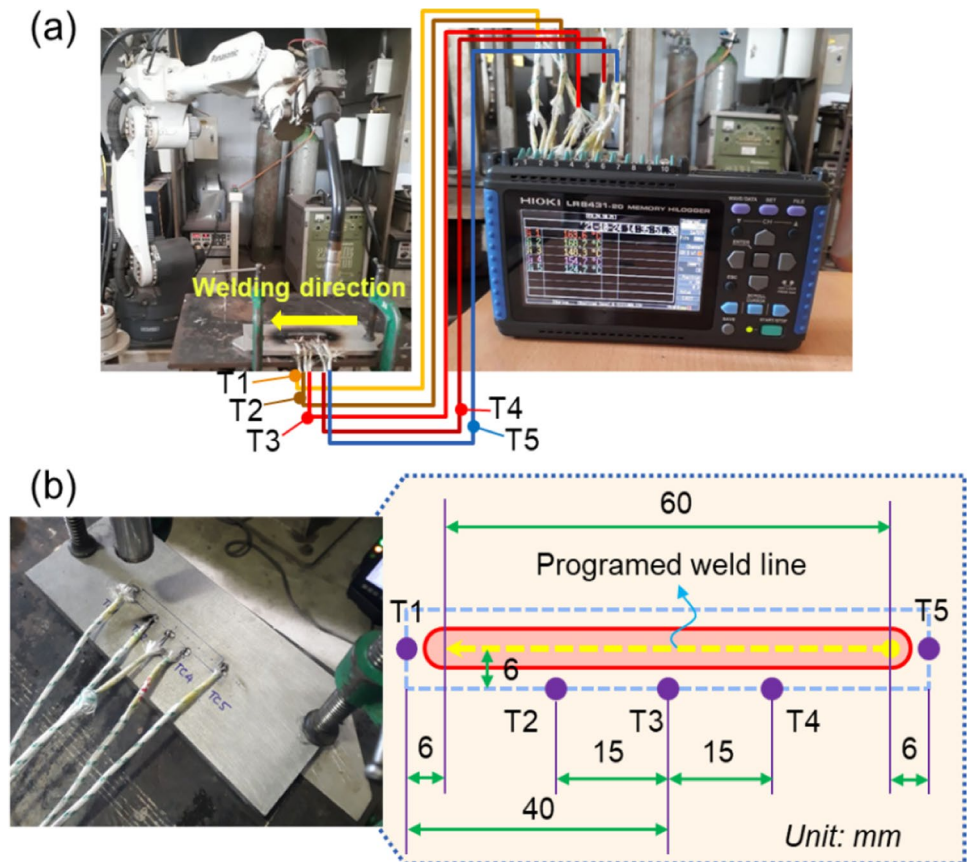
made of 316L stainless steel (316L SS) with an industrial GMAW welding robot: TA1400 Panasonic. The 316L SS wire with 1.2 mm in diameter was utilized. The chemical composition of the wire and substrate material includes 0.01% C, 0.59% Si, 1.53% Mn, 18.56% Cr, 11.55% Ni, 2.53% Mo, and balance of Fe (in wt. %) (Lee 2020). The thermal properties of 316L SS including density, specific heat, and thermal conductivity were estimated from its chemical composition using JMatPro software, as shown in Fig. 1.

2.2 Experimental set-up

A single weld track was performed on the 316L SS substrate (Fig. 2a). The main parameters, including a travel speed of the weld torch $V=0.4$ m/min, a welding current $I=110$ A, and a voltage $U=23$ V, were utilized. A shielding gas of pure argon with 20 L/min in flow rate was applied during the WAAM process.

The temperature evolutions at five points on the substrate surface were recorded using five K-type thermocouples and a HIOKI LRB431-20 Memory HiLoggers machine (see Fig. 2a). The positions of the thermocouples were carefully attached to the measurement positions by the TIG welding

Fig. 2 a Experimental set-up for capturing the thermal evolution at five points on the substrate surface by the thermocouples. b Positions of five thermocouples (T1 to T5)



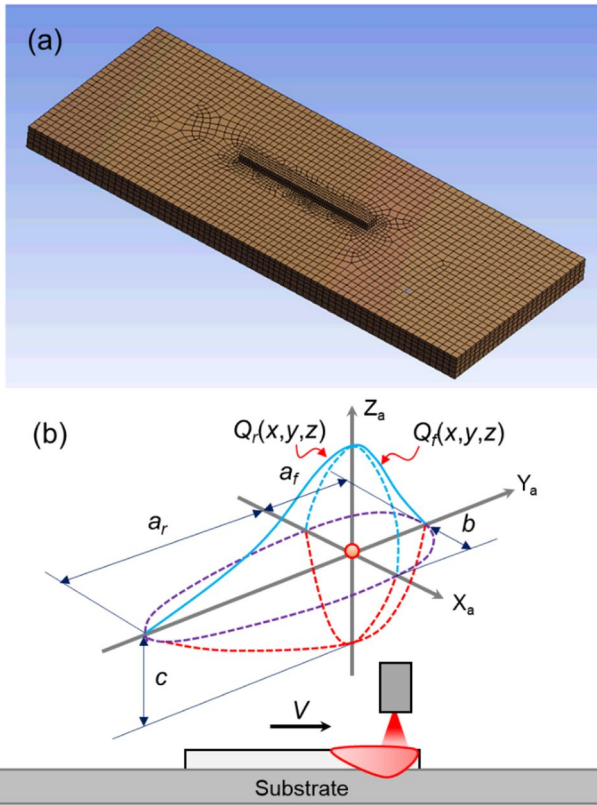
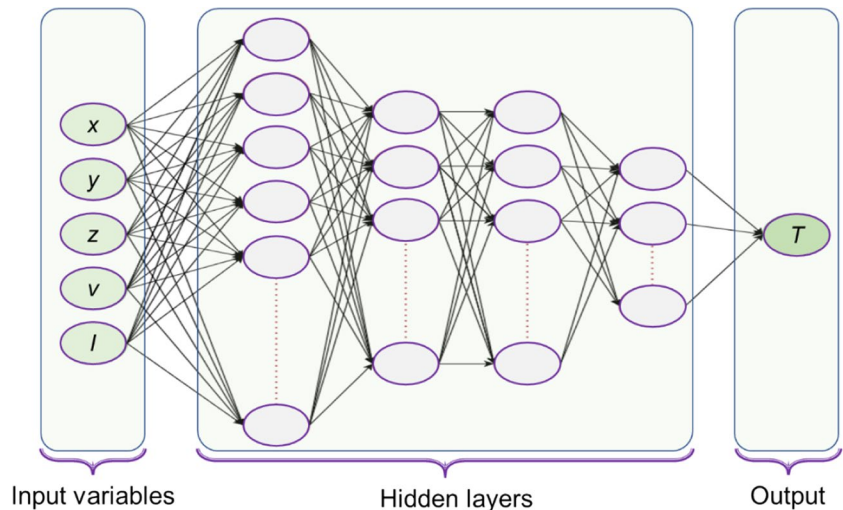


Fig. 3 a Finite element mesh. b Goldak’s model for the energy source

Table 1 Datasets obtained from the FE simulations used to develop the FFNN model

Current I (A)	110	120	130	140	150
Travel speed V (m/min)	0.3	0.4	0.5	0.6	0.7
Training data	✓	✓		✓	✓
Testing data			✓		

Fig. 4 A general FFNN’s architecture used in this study



process as shown in Fig. 2b. These measurements are used to validate the temperature evolution at the identical points extracted from the FE model, which is modeled under the same process parameters.

2.3 Finite element model

Thermal analysis of a single weld track in the WAAM process is performed by ANSYS software. The temperature evolution is governed by the following equation [33]:

$$\frac{\partial}{\partial x}(K \frac{\partial T}{\partial x}) + \frac{\partial}{\partial y}(K \frac{\partial T}{\partial y}) + \frac{\partial}{\partial z}(K \frac{\partial T}{\partial z}) + \dot{Q} = \rho C_p (\frac{\partial T}{\partial t} - V \frac{\partial T}{\partial x}) \tag{1}$$

where T and K are the temperature and thermal conductivity, respectively; ρ is the material density, C_p is the specific heat, V is the speed of heat source, and \dot{Q} is the volume heat source. In this work, ρ , K , and C_p are the functions of temperature as reported in Fig. 1.

It is assumed that the initial temperatures (denoted by T_{ini}) of the testing environment and the substrate are equal to 25 °C. The boundary conditions of convection and radiation on the surfaces are described by Eq. (2).

$$-\langle \frac{\partial T}{\partial x}, \frac{\partial T}{\partial y}, \frac{\partial T}{\partial z} \rangle \cdot \vec{n} = \epsilon \sigma (T^4 - T_{ini}^4) + h(T - T_{ini}) \tag{2}$$

where σ is the Stefan-Boltzmann constant, $\sigma = 5.67 \times 10^{-8} \text{ W.m}^{-2}.\text{K}^{-4}$ [34]; ϵ is the emissivity coefficients of the sample surfaces, $\epsilon = 0.9$ [17]; \vec{n} depicts the unitary normal vector of the surfaces; h is the local heating exchange coefficient, $h = 30 \text{ W.m}^{-2}.\text{K}^{-1}$ [17]. Moreover, we also used $h = 400 \text{ W.m}^{-2}.\text{K}^{-1}$ for the substrate surface that contacts the building table [33].

Figure 3a shows the finite element mesh of the simulation which contains 3225 hexahedral elements and 3563 nodes. The weld bead track was simulated by a volume of $L \times W \times H$

Table 2 Testing results with different architectures of the FFNN model

No	Layer 1	Layer 2	Layer 3	Layer 4	Final MSE	R ²
1	400	300	250	200	6.22×10 ⁻⁵	0.9936
2	300	200	150	100	4.66×10 ⁻⁵	0.9922
3	250	200	150	100	4.12×10 ⁻⁵	0.9931
4	220	160	140	100	4.1×10 ⁻⁵	0.9938

(in length × width × height, respectively) and a mesh size of 1.4 mm × 1.4 mm × 1.4 mm was used. The values of *L*, *W*, and *H* were measured from the fabricated weld track. The mesh size of 3 mm × 3 mm × 3 mm is used in the substrate to reduce the computing time. The birth and death method [35] was used during the deposition.

The heat source (Fig. 3b) is modeled using the Goldak model [36]. For the material points in the first half-ellipsoid in front of the welding arc, the heat flux is considered by Eq. (3), while the heat flux for the points in the last half-ellipsoid located in the rear part of the arc is described by Eq. (4).

$$Q_f(x, y, z) = \frac{6\sqrt{3}f_f Q}{a_f b c \pi \sqrt{\pi}} \exp\left(-\frac{3x^2}{a_f^2} - \frac{3y^2}{b^2} - \frac{3z^2}{c^2}\right) \quad (3)$$

$$Q_r(x, y, z) = \frac{6\sqrt{3}f_r Q}{a_r b c \pi \sqrt{\pi}} \exp\left(-\frac{3x^2}{a_r^2} - \frac{3y^2}{b^2} - \frac{3z^2}{c^2}\right) \quad (4)$$

where *a_r*, *a_f*, *b*, and *c* are constants (see Fig. 3b), *f_r* and *f_f* depict the proportion of the heat input in the rear and front sides satisfying *f_f* = 0.6 and *f_r* = 1.4, and *Q* = *η* × *I* × *U* is the heat input with *η*, *I*, and *U* the arc efficiency ratio, the current, and the voltage, respectively. In this work, *a_f* = 7 mm, *a_r* = 13 mm, *b* = 4 mm, *c* = 4 mm [37], and *η* = 0.8 [38] were used.

2.4 Machine learning-based surrogate model

In this section, we introduce the machine learning-based surrogate model to replace the FE model to predict the temperature evolutions of WAAM process. The ML surrogate model is chosen based on the following two steps:

- (i) Data collection: generating a set of input–output pairs, i.e., the current *I*, the travel speed *V*, and temperature by running high fidelity FE model.
- (ii) Choosing an appropriate ML algorithm and optimizing its hyperparameters.

For step (i), five datasets obtained from the FE-based thermal simulations were collected and separated into two categories—four datasets for the model training and one dataset for model testing (Table 1). The FE simulations generated these five datasets using different values of the process variables (the current *I* and the travel speed *V*) while the voltage *U* was fixed at 20 V. In detail, the training and testing datasets contain the temperature fields of all mesh points of the weld track and substrate sample. Each training dataset includes 21,898 data points for the nodes with 420 steps of time, resulting in 36,788,640 data points for the training dataset. Each node presents a temperature curve *T*(*t*). Similarly, the dataset for the testing of the model contains 9,197,160 data points. In addition, the FE-based thermal

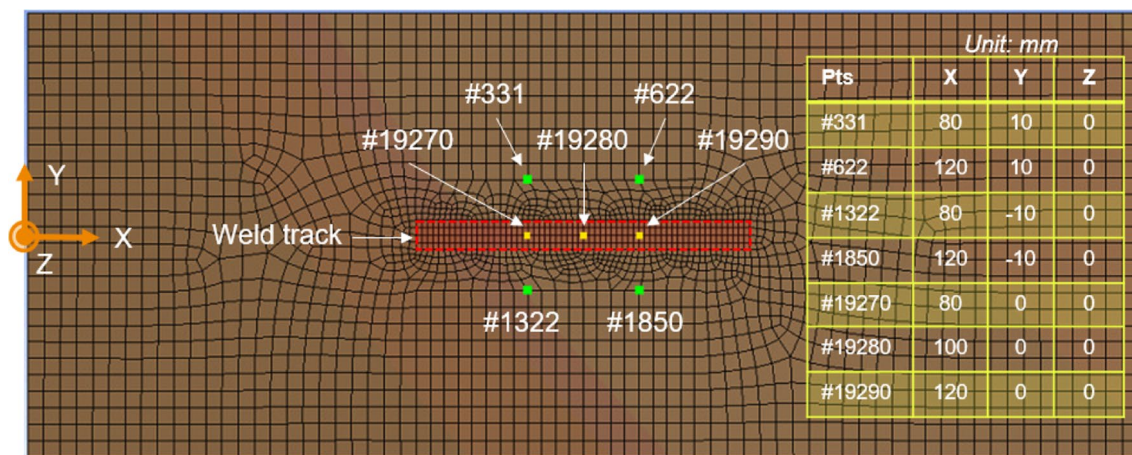


Fig. 5 The points used to assess the prediction accuracy of the FFNN model vs. the FE model

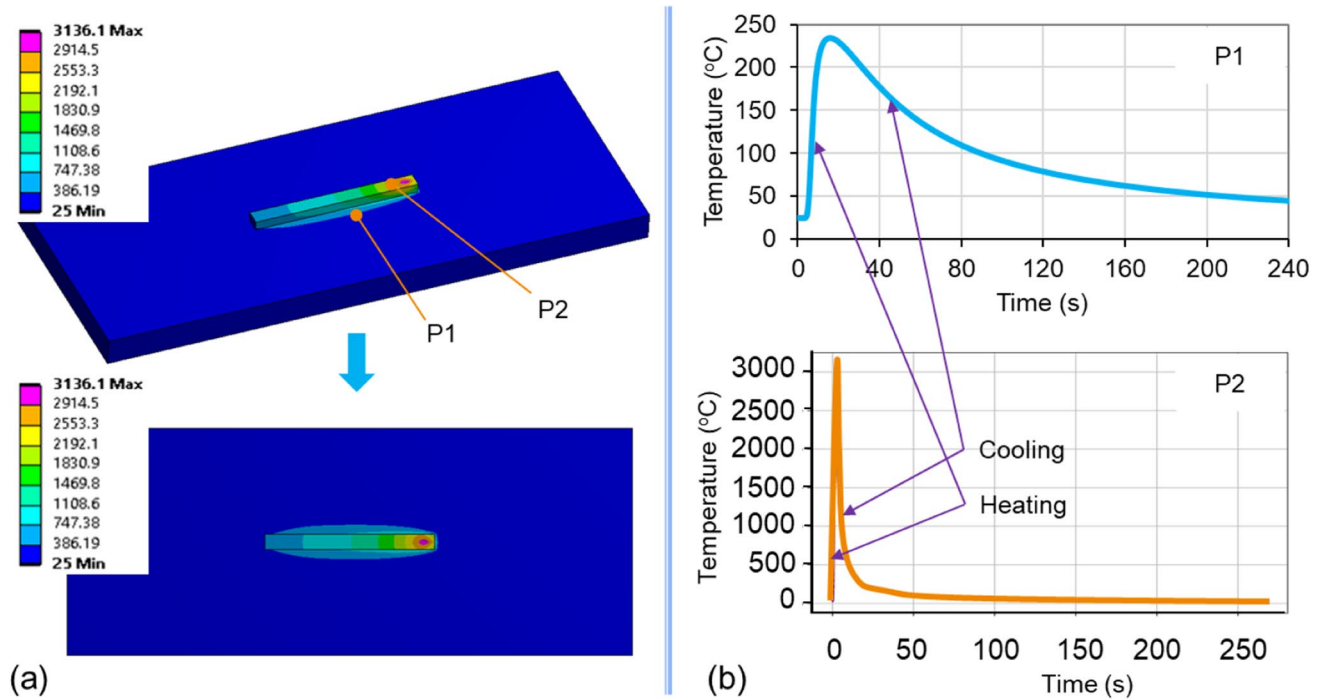


Fig. 6 Thermal field achieved by the FE model. **a** Temperature field. **b** Temperature evolutions

simulations and the extraction of datasets were performed on a computer with the configuration of Intel i7 6700 CPU for the processor, 32 GB RAM for the memory, and NVIDIA GeForce GTX-1660Ti for the GPU.

For step (ii), there are several methods that can be applied such as linear regression, polynomial regression, and feed-forward neural networks (FFNN). In this study, we choose the FFNN architecture to construct the surrogate model to gain the advantages of approximating highly non-linear and high-dimensional function of the physics inside WAAM process.

FFNN is the simplest form of an artificial neuron as the information feeds forward in the network, i.e., through input nodes, hidden layers, and output nodes. To predict the output, each neuron performs a dot product of the input and its corresponding weights, together with the addition of the bias and the application of a nonlinearity activation function.

In this study, the input variables are composed of the coordinates (x, y, z) of a mesh point, the travel speed V , and the current I , while the model's output is the predicted temperature T at the considered mesh point. The number of hidden layers was fixed at four layers (Fig. 4).

The training process of the FFNN model consists of optimizing its weight and bias matrices by minimizing a predefined loss function, namely the mean squared error (MSE). Meanwhile, the hyperparameters were optimized through several training and cross-validation processes to ensure the best model performance. The EarlyStopping callback was used to avoid model overfitting, and the model weight and

bias matrices can be saved using ModelCheckpoint callback. The EarlyStopping callback was used to avoid model overfitting, and the model weight and bias matrices can be saved using ModelCheckpoint callback. The weights and biases (W) are determined by resolving the minimization problem of mean squared error (MSE) loss, as Eq. (5).

$$MSE = \frac{1}{N} \sum_{i=1}^N (\mathfrak{F}(d^{(i)}|W) - T^{(i)})^2 \quad (5)$$

where N is the training data number, \mathfrak{F} is the FFNN model, $d = [x, y, z, V, I]$ is the input vector, and $T^{(i)}$ is the temperature corresponding to each input vector $d^{(i)}$.

To evaluate the model performance, the coefficient of determination R^2 , Eq. (6) was used.

$$R^2 = 1 - \frac{\sum_{i=1}^N (T_i - \tilde{T}_i)^2}{\sum_{i=1}^N (T_i - \bar{T})^2} \quad (6)$$

where \tilde{T}_i is the predicted value of T_i , and \bar{T} is the mean value of T_i .

In this study, several structures with different numbers of hidden layers and different numbers of neurons in each hidden layer (Table 2) were tested with the datasets given in Table 1. After evaluating the model performance, the most appropriate FFNN model which shows the highest R^2 value was selected.

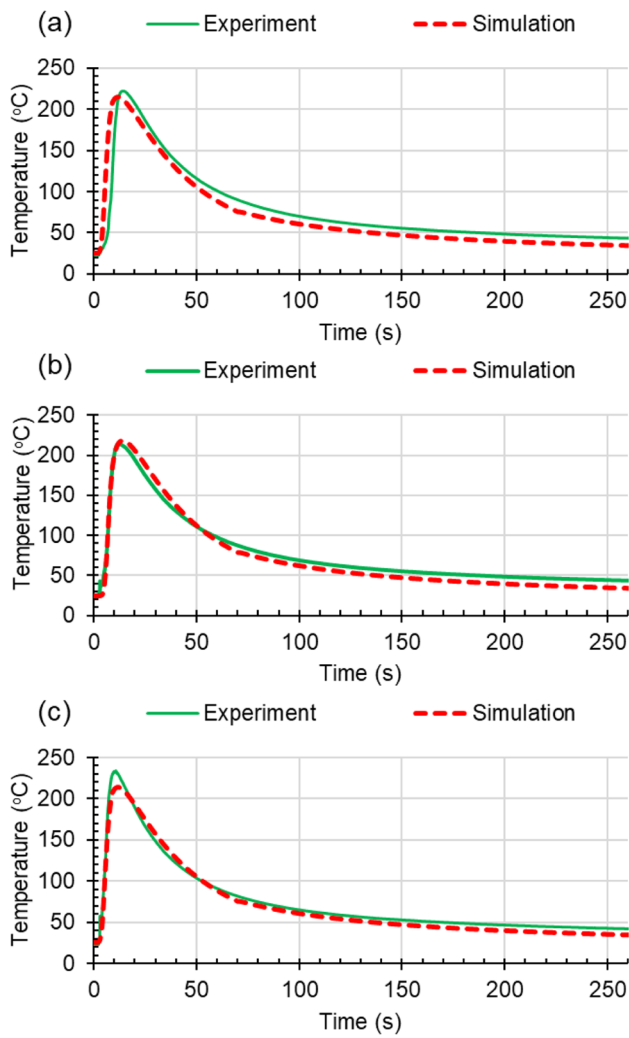


Fig. 7 Comparison of thermal evolution obtained by the experiment and the simulation at positions **a** T2, **b** T3, and **c** T4 (see Fig. 3)

In addition to the coefficient of determination R^2 , we also considered MAE (the mean of absolute errors) (Eq. (7)) and RMSE (root mean squared error) (Eq. (8)) to evaluate the robustness of the selected model for the temperature evolution prediction in the entire part and at several specific points.

$$MAE = \frac{1}{N} \sum_{i=1}^N |T_i - \tilde{T}_i| \tag{7}$$

$$RMSE = \sqrt{\frac{1}{N} \sum_{i=1}^N (T_i - \tilde{T}_i)^2} \tag{8}$$

Figure 5 shows the positions to assess the FFNN model’s accuracy versus the FE model. We selected three points on the center line of the weld track (i.e., the points

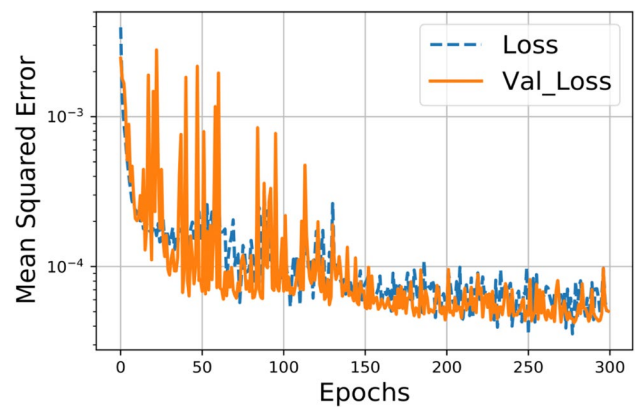


Fig. 8 Results on the training and validation losses of the FFNN model

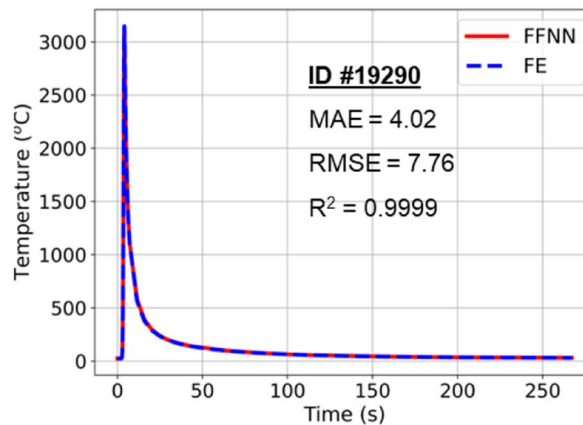
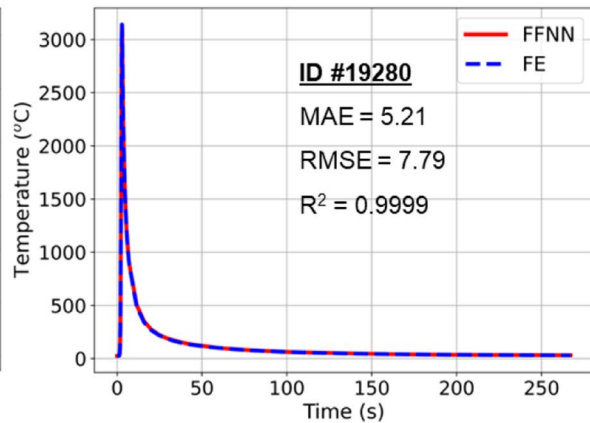
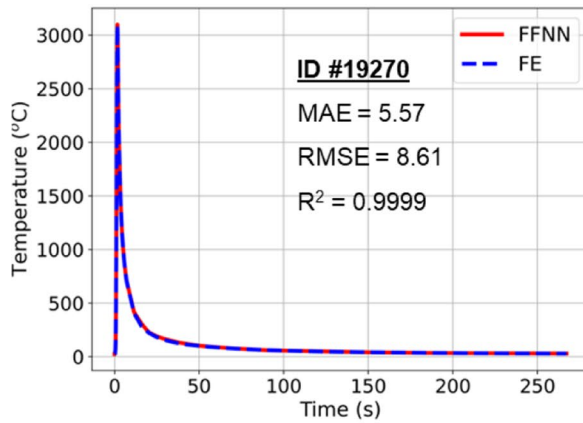
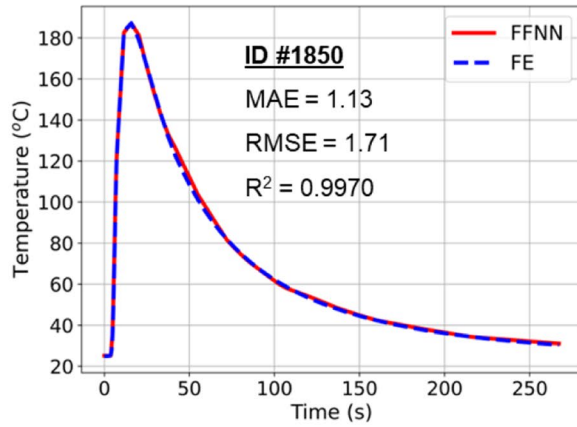
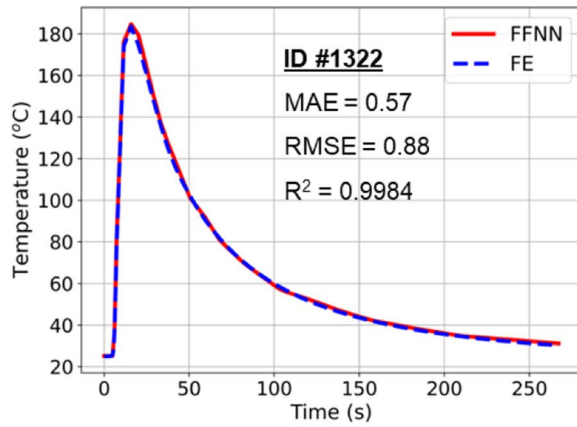
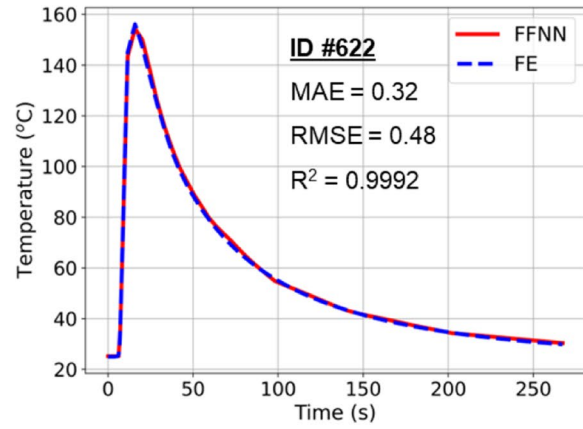
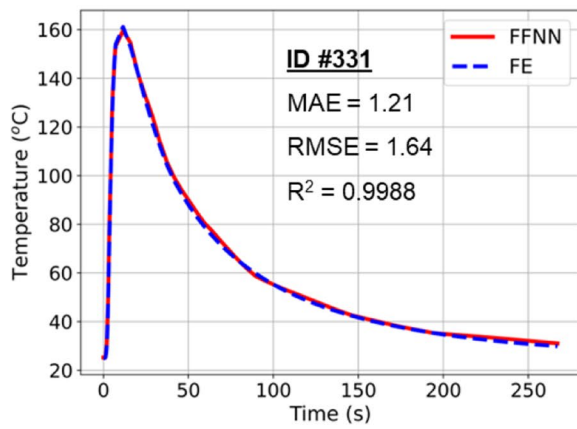
ID #19,270, #19,280, and #19,280) to observe the temperature history in the fusion zone. Moreover, two points on each side on the top surface of the substrate close to the weld track (i.e., the points ID #331, #622, #1322, and #1850) were also examined. The thermal evolutions at these points (ID #331 to #1850) are similar to those observed by the thermocouples in the experiment.

3 Results and discussion

3.1 FE and experiment results

Figure 6 shows the thermal field achieved by the FE model. As shown in Fig. 6a, the heat source is moving during the deposition process. As shown in Fig. 6b, the temperature evolution typically consists of a heating phase in which the heat source moves to the observed point and a cooling phase in which the heat source passes the observed point. For the point of the weld track (P2), a high-temperature peak (up to over 3000 °C) is observed, followed by first a rapid cooling part and then a long slow cooling part, while in the case of the point (P1) on the substrate close to the weld track, the temperature peak is much lower. For the solidification process of the melted metal, the rapid cooling part of the temperature cycle curve is important, because it significantly influences the microstructures and the mechanical characteristics of the as-deposited material [23, 39].

In the experiment, we recorded the temperature evolution at five points on the substrate by five thermocouples T1 to T5 (Fig. 2). However, only the temperature data recorded by T2, T3, and T4 were exploitable, because the results observed from these thermocouples nearly repeated at least three times in the five repeated experiments. On the other hand, the results observed from the thermocouples T1 and T5 were variable in the five repeated experiments. This may



◀**Fig. 9** Comparison between the temperatures predicted by the FFNN and FE models at the studied points

be caused by the imperfection and defects of welding the T1 and T5 on the substrate. Therefore, we decided to exclude T1 and T5 in the validation.

Figure 7 shows the comparison between the temperature history obtained with the FE simulation and with the experiment at the measuring points of the thermocouples T2, T3, and T4. The simulated temperature curves were good in line with the measured temperature curves in terms of the profile and values. The RMSE values between the simulated and measured temperatures were about 25.52, 24.87, and 28.63 °C at points T2, T3, and T4, respectively. The relative errors of peak temperature between the experiment and the simulation are 3.26% (in Fig. 7a), 1.87% (in Fig. 7b), and 9.35% (in Fig. 7c). During the slow cooling to room temperature (e.g., from 100 s in all three cases), the temperature discrepancy is inferior to 1 °C (corresponding to a relative error between two solutions is inferior to 2%). These results demonstrated that the FE model was validated accurately by the experiment.

The errors between the simulation and experiment may relate to the FE model error, the uncertainty in the process parameters, and the unknown physical properties of the material. The model predictability could be enhanced by calibrating the parameters of the heat source (as shown in

Fig. 3b), the weld bead shape, and the refinement of the finite element mesh. However, these tasks were time-consuming because they caused a significant increase in the computation time, the efforts of modeling, and the experimental runs. The results obtained from Fig. 7 show that the FE model can be generally considered to be validated against experiments.

3.2 Results of the FFNN model

It is noticed that the normalization of data to the values between 0 and 1 was applied before training the model to prevent the unfavorable influence of the discrepancy in input variable units and improve the convergence and performance of the model. Thereafter, four datasets of the training category described in step (i) were randomly divided into the training and cross-validation sets with a ratio of 80% and 20%, respectively, and one dataset (corresponding to $I=130$ A and $V=0.5$ m/min) was used for the performance testing.

Table 2 shows the testing results with different architectures of the FFNN model. As a result, the selected numbers of neurons in the first to the fourth hidden layers of the FFNN model were 220, 160, 140, and 100, respectively (Table 2) with the smallest final MSE ($=4.1 \times 10^{-5}$) and the highest value of R^2 ($=0.9938$).

Figure 8 presents the losses of training and validation of the FFNN-SM. The training ends at 300th epoch because there is no considerable reduction in validation loss, thus

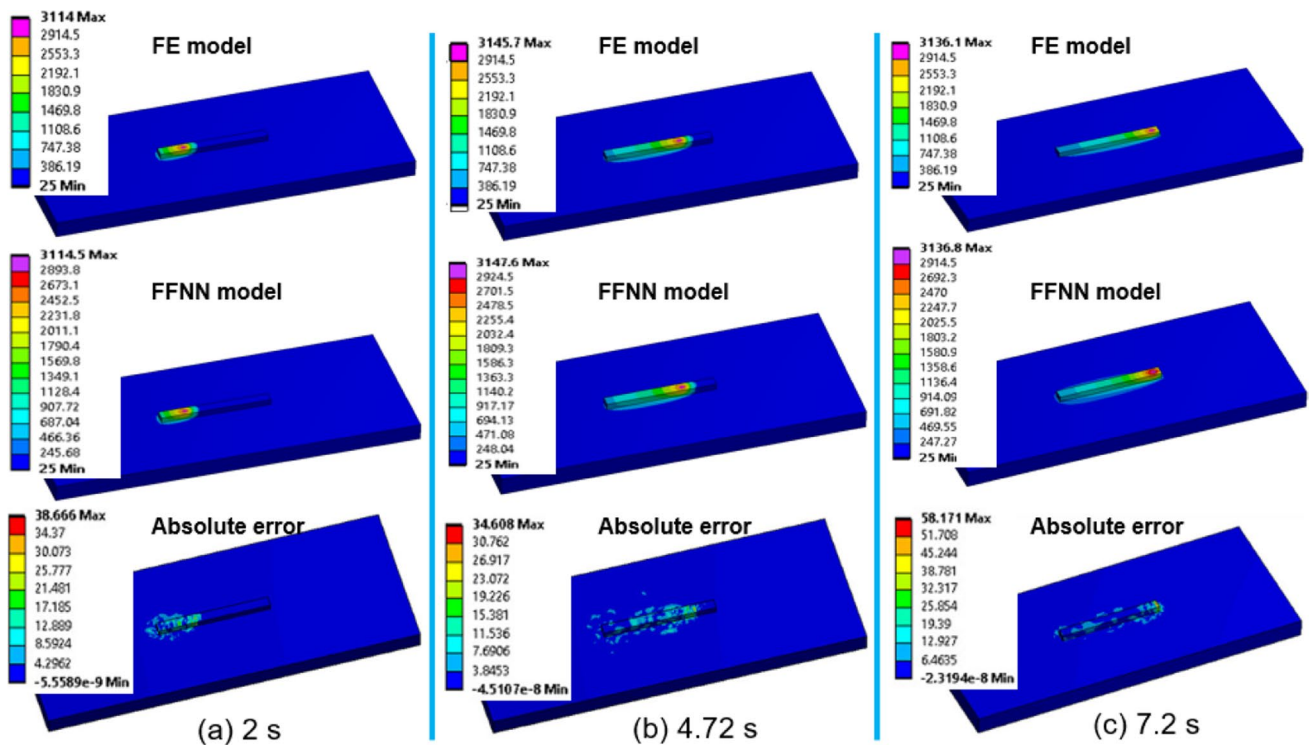


Fig. 10 Comparison between the temperature fields predicted by the FFNN and FE models for the entire part at **a** 2 s, **b** 4.72 s, and **c** 7.2 s

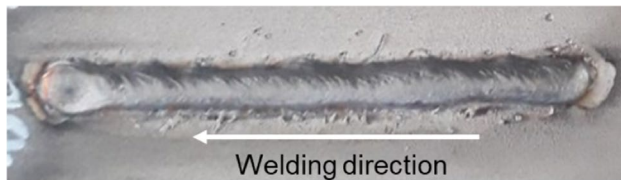


Fig. 11 Weld track fabricated with $I=120$ A, $V=0.3$ m/min, and $U=20$ V

ensuring a reliable training procedure. Note that some large peaks observed in Fig. 8 are unavoidable consequences of the Mini Batch Gradient Descent strategy in the Adam optimizer of the FFNN training procedure. Since our dataset consists of more than 36 million data points, we accept the trade-off of using the mini-batch strategy but observe a couple of peaks during training which does not affect the predicting accuracy. Hereafter, we use the model “No. 4” to perform the temperature prediction.

3.3 Comparison of the FFNN model with the FE model

To evaluate the capability of FFNN as a surrogate model of the FE, a comparison between the FFNN and FE models was carried out in terms of the accuracy and the computational time in the new case of $\{I=130$ A and $V=0.5$ m/min $\}$ which was not previously used for training. For assessing the accuracy, the temperatures predicted by the FFNN model and the FE simulation were compared in two aspects: the temperature history at several studied points (Fig. 5) and the thermal field in the whole space of the weld track and the substrate at specific moments of the deposition.

Figure 9 shows the temperature curves for the observed points that were depicted in Fig. 5. It is indicated that, at all points, the temperature curves reveal the heating and cooling characteristics for the case of a single track. Moreover, the temperature curves predicted by the FFNN model and those obtained by the FE simulations are nearly identical. For example, for the points on the substrate close to the weld track, the values of R^2 coefficient were over 0.9970, and the MAE and RMSE in temperature between the two models were lower than 2 °C. Particularly, for the studied points (ID#19,270 to ID#19,290) on the weld track, the values of R^2 coefficient were superior to 0.9999. On the other hand, the MAE and RMSE in temperature between the two models were relatively higher than those at the points on the substrate, but these error metric values were also low and inferior to 6 °C and 9 °C, respectively. As a result, it can be concluded that the FFNN model not only captures the temperature curve characteristics, but also mimics the results generated by the FE model with a very high accuracy.

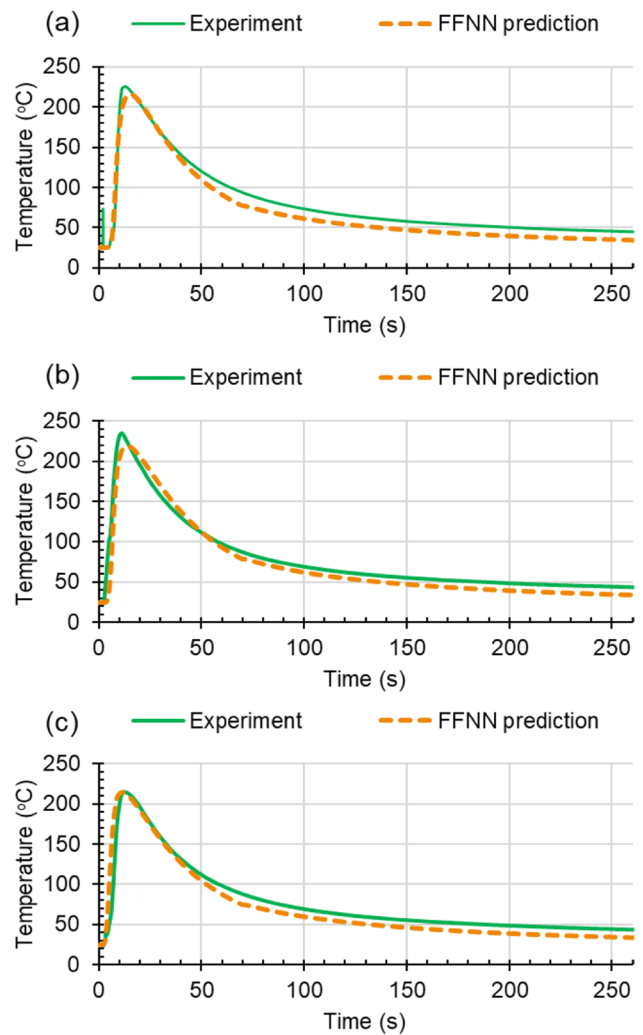


Fig. 12 Comparison between the temperature predicted by the FFNN and the confirmation experiment for a weld track of $I=120$ A, $V=0.3$ m/min, and $U=20$ V at positions **a** T1, **b** T3, and **c** T4

Figure 10 shows the comparison results in the temperature field between the two models at several moments of deposition (i.e., $t=2$ s, 4.72 s, and 7.2 s). From the temperature distribution, the temperature gradient along the deposition direction was observed. At all moments of deposition, the FFNN model well captured the results of the FE model with high accuracy (e.g., $R^2=0.9967$, MAE=0.65 °C, and RMSE=1.83 °C). These results again

Table 3 Computation time comparison between the FFNN and FE models

Model	Running time to create training dataset	Training time	Single temperature evaluation
FFNN model	20 h	6 h	38 s
FE model	-	-	5 h

show the perfect accordance of the FFNN model with the FE model.

3.4 Comparison of the FFNN model with the experiment

To confirm the reliability of the FFNN model, a similar experiment was set up (as shown in Fig. 2) with the following set of process variables: $I = 120$ A, $V = 0.3$ m/min, and $U = 20$ V. The fabricated weld track is shown in Fig. 11. Subsequently, the temperatures measured by thermocouples T1 to T5 were compared with those predicted by the FFNN model to verify the accuracy of the prediction model.

The temperature predicted by the FFNN model was also compared to that measured by the thermocouple in the confirmation test ($I = 120$ A, $V = 0.3$ m/min, and $U = 20$ V). As shown in Fig. 12, the temperature curves predicted by the FFNN model were in good agreement with the measured temperature curves. Some discrepancies between the experiment and FFNN model can be observed in Fig. 12, but they are acceptable. For example, the difference in the peak temperature is about 10 °C and 9 °C in Fig. 12 a and b, respectively. Namely, the relative error of peak temperature is inferior to 8%. The discrepancy in temperature during the slow cooling part to room temperature between two models is also small, inferior to 12 °C. The RMSE values between the totally simulated and measured temperature curves were about 24.73, 26.38, and 16.85 °C at points T1 (Fig. 12a), T3 (Fig. 12b), and T4 (Fig. 12c), respectively. The errors between the FFNN and experiment could be related to the difference in the measuring positions between the measured points in the experiment and the points' IDs in the FFNN model. Practically, the temperature curve can be only extracted at each mesh point of the simulation model, while the measured point in the experiment and that point in the mesh model are not identical. Moreover, as mentioned above, the environmental conditions and the quality of attaching the thermocouples on the substrate surface significantly influence the measurement results, while the temperature predicted by the FFNN model is based on the numerical data generated by the FE model. This also causes the errors between the FFNN model and the experiment. However, with the consistency in the thermal curve form and the acceptable RMSE levels between the FFNN and the experiment, it is considered that the FFNN model is validated against experiments. To improve the consistency between the experiment and the simulation models, the step of calibrating the simulation model is very important. However, it is difficult to obtain a perfect model because of the sensibility of the experimental conditions, while the condition boundary of the simulation is ideal. Therefore, in most of the published works, the authors considered that

the predicted results of their model are acceptable when the thermal cycle curve is captured in shape and the error values (e.g., MAE and RMSE) fall in a permitted range [31, 32].

3.5 Comparison of the computation time of the FFNN model vs. the FE model

Table 3 shows the computation cost of the FE and FFNN models. To create the training dataset, the four simulations have been carried out, as shown in Table 1. Each simulation required a total time of about 5 h. Therefore, the total time needed to build the training dataset is approximately 20 h. The training time of the FFNN model is 6 h. After that, the FFNN model can rapidly predict the temperature within only 38 s, resulting in a reduction of 473 times compared to the FE model. If only several simulations are required, the FFNN model does not show its benefits compared to the FE model. However, when a large number of simulations need to be performed, for example, for the quantification of uncertainty and the processing optimization, the FFNN provides a tremendous advantage in terms of computing time.

4 Conclusions

In this paper, an efficient SM framework using a combination of machine learning and numerical simulation for predicting the thermal history in the WAAM process of single weld tracks was developed. The SMs are trained by the dataset obtained from the FE-based thermal simulation, which was validated against experiment. The trained SM model can fast and accurately predict the temperature history in the cases which were not previously used for training with a very high accuracy of more than 99% and in a very short time with only 38 s (after being trained) as compared with 5 h for a FE model.

Although the FFNN-SM was developed for the WAAM process of single weld tracks—the first step of our project on developing SM to rapidly and accurately predict temperature field of the whole part fabricated by the WAAM process based the simulation data, the approach presented in this paper could be used for predicting thermal evolution in the deposition of multi-tracks and multi-layers in WAAM and other AM processes (e.g., DED process [40]). Moreover, the SM development can open the approach towards obtaining real-time monitoring in AM. In future works, we will attempt to apply this approach for the WAAM process of single-track multi-layer or multi-track multi-layer components. Moreover, the current SM was developed with a fixed path planning. Therefore, the variation of the path planning in the WAAM process will be considered when developing the future SM.

Author contribution Van Thao Le: conceptualization, methodology, data curation, experiment, investigation, formal analysis, writing – original draft and editing; Manh Cuong Bui: methodology, simulation, visualization; Thinh Quy Duc Pham: formal analysis, investigation, methodology, writing – original draft; Hoang Son Tran: methodology, supervision; Xuan Van Tran: funding acquisition, writing – review and editing.

Funding This work was funded by Vingroup and supported by the Vingroup Innovation Foundation (VINIF) under project code VINIF.2020.DA15.

Declarations

Conflict of interest The authors declare no competing interests.

References

- Thompson MK, Moroni G, Vaneker T et al (2016) Design for additive manufacturing: trends, opportunities, considerations, and constraints. *CIRP Ann Manuf Technol* 65:737–760. <https://doi.org/10.1016/j.cirp.2016.05.004>
- Betzler BR (2021) Additive manufacturing in the nuclear reactor industry. In: Greenspan E (ed) *Encyclopedia of nuclear energy*. Elsevier, pp 851–863. <https://doi.org/10.1016/B978-0-12-819725-7.00106-9>
- Altıparmak SC, Xiao B (2021) A market assessment of additive manufacturing potential for the aerospace industry. *J Manuf Process* 68:728–738. <https://doi.org/10.1016/j.jmapro.2021.05.072>
- Madhavadas V, Srivastava D, Chadha U et al (2022) A review on metal additive manufacturing for intricately shaped aerospace components. *CIRP J Manuf Sci Technol* 39:18–36. <https://doi.org/10.1016/j.cirpj.2022.07.005>
- Le VT, Paris H, Mandil G (2018) The development of a strategy for direct part reuse using additive and subtractive manufacturing technologies. *Addit Manuf* 22:687–699. <https://doi.org/10.1016/j.addma.2018.06.026>
- Thompson SM, Bian L, Shamsaei N, Yadollahi A (2015) An overview of direct laser deposition for additive manufacturing; Part I: Transport phenomena, modeling and diagnostics. *Addit Manuf* 8:36–62. <https://doi.org/10.1016/j.addma.2015.07.001>
- Shamsaei N, Yadollahi A, Bian L, Thompson SM (2015) An overview of direct laser deposition for additive manufacturing; Part II: Mechanical behavior, process parameter optimization and control. *Addit Manuf* 8:12–35. <https://doi.org/10.1016/j.addma.2015.07.002>
- Liu J, Xu Y, Ge Y et al (2020) Wire and arc additive manufacturing of metal components: a review of recent research developments. *Int J Adv Manuf Technol* 111:149–198. <https://doi.org/10.1007/s00170-020-05966-8>
- Jafari D, Vaneker THJ, Gibson I (2021) Wire and arc additive manufacturing: opportunities and challenges to control the quality and accuracy of manufactured parts. *Mater Design* 202:109471. <https://doi.org/10.1016/j.matdes.2021.109471>
- Williams SW, Martina F, Addison AC et al (2016) Wire + arc additive manufacturing. *Mater Sci Technol* 32:641–647. <https://doi.org/10.1179/1743284715Y.0000000073>
- Le VT, Mai DS, Paris H (2021) Influences of the compressed dry air-based active cooling on external and internal qualities of wire-arc additive manufactured thin-walled SS308L components. *J Manuf Process* 62:18–27. <https://doi.org/10.1016/j.jmapro.2020.11.046>
- Rodrigues TA, Cipriano Farias FW, Zhang K et al (2022) Wire and arc additive manufacturing of 316L stainless steel/Inconel 625 functionally graded material: development and characterization. *J Market Res* 21:237–251. <https://doi.org/10.1016/j.jmrt.2022.08.169>
- Zuo X, Zhang W, Chen Y et al (2022) Wire-based directed energy deposition of NiTiTa shape memory alloys: microstructure, phase transformation, electrochemistry, X-ray visibility and mechanical properties. *Addit Manuf* 59:103115. <https://doi.org/10.1016/j.addma.2022.103115>
- Ramalho A, Santos TG, Bevans B et al (2022) Effect of contaminations on the acoustic emissions during wire and arc additive manufacturing of 316L stainless steel. *Addit Manuf* 51:102585. <https://doi.org/10.1016/j.addma.2021.102585>
- Cunningham CR, Flynn JM, Shokrani A et al (2018) Invited review article: strategies and processes for high quality wire arc additive manufacturing. *Addit Manuf* 22:672–686. <https://doi.org/10.1016/j.addma.2018.06.020>
- Tomar B, Shiva S, Nath T (2022) A review on wire arc additive manufacturing: processing parameters, defects, quality improvement and recent advances. *Mater Today Commun* 31:103739. <https://doi.org/10.1016/j.mtcomm.2022.103739>
- Ding J, Colegrove P, Mehnen J et al (2011) Thermo-mechanical analysis of wire and arc additive layer manufacturing process on large multi-layer parts. *Comput Mater Sci* 50:3315–3322. <https://doi.org/10.1016/j.commatsci.2011.06.023>
- Zhao H, Zhang G, Yin Z, Wu L (2011) A 3D dynamic analysis of thermal behavior during single-pass multi-layer weld-based rapid prototyping. *J Mater Process Technol* 211:488–495. <https://doi.org/10.1016/j.jmatprotec.2010.11.002>
- Li S, Li JY, Jiang ZW et al (2022) Controlling the columnar-to-equiaxed transition during directed energy deposition of Inconel 625. *Addit Manuf* 57:102958. <https://doi.org/10.1016/j.addma.2022.102958>
- Rodrigues TA, Escobar JD, Shen J et al (2021) Effect of heat treatments on 316 stainless steel parts fabricated by wire and arc additive manufacturing : microstructure and synchrotron X-ray diffraction analysis. *Addit Manuf* 48:102428. <https://doi.org/10.1016/j.addma.2021.102428>
- Wu B, Pan Z, Ding D et al (2018) A review of the wire arc additive manufacturing of metals: properties, defects and quality improvement. *J Manuf Process* 35:127–139. <https://doi.org/10.1016/j.jmapro.2018.08.001>
- Yang D, Wang G, Zhang G (2017) Thermal analysis for single-pass multi-layer GMAW based additive manufacturing using infrared thermography. *J Mater Process Technol* 244:215–224. <https://doi.org/10.1016/j.jmatprotec.2017.01.024>
- Rodrigues TA, Duarte V, Avila JA et al (2019) Wire and arc additive manufacturing of HSLA steel: effect of thermal cycles on microstructure and mechanical properties. *Addit Manuf* 27:440–450. <https://doi.org/10.1016/j.addma.2019.03.029>
- Le VT, Mai DS, Bui MC et al (2022) Influences of the process parameter and thermal cycles on the quality of 308L stainless steel walls produced by additive manufacturing utilizing an arc welding source. *Weld World* 66:1565–1580. <https://doi.org/10.1007/s40194-022-01330-4>
- Le VT, Bui MC, Nguyen TD et al (2023) On the connection of the heat input to the forming quality in wire-and-arc additive manufacturing of stainless steels. *Vacuum* 209:111807. <https://doi.org/10.1016/j.vacuum.2023.111807>
- Xie X, Bennett J, Saha S et al (2021) Mechanistic data-driven prediction of as-built mechanical properties in metal additive manufacturing. *npj Comput Mater* 7:86. <https://doi.org/10.1038/s41524-021-00555-z>
- Johnson NS, Vulimiri PS, To AC et al (2020) Invited review: machine learning for materials developments in metals additive

- manufacturing. *Addit Manuf* 36:101641. <https://doi.org/10.1016/j.addma.2020.101641>
28. Zhu Q, Liu Z, Yan J (2021) Machine learning for metal additive manufacturing: predicting temperature and melt pool fluid dynamics using physics-informed neural networks. *Comput Mech* 67:619–635. <https://doi.org/10.1007/s00466-020-01952-9>
 29. Pham QDT, Hoang TV, Pham QT et al (2021) Data-driven prediction of temperature evolution in metallic additive manufacturing process. *Esaform* 13:1–10. <https://doi.org/10.25518/esaform21.2599>
 30. Fetni S, Pham QDT, Tran VX et al (2021) Thermal field prediction in DED manufacturing process using artificial neural network. *ESAFORM 2021* 13:1–10. <https://doi.org/10.25518/esaform21.2812>
 31. Roy M, Wodo O (2020) Data-driven modeling of thermal history in additive manufacturing. *Addit Manuf* 32:101017. <https://doi.org/10.1016/j.addma.2019.101017>
 32. Mozaffar M, Paul A, Al-Bahrani R et al (2018) Data-driven prediction of the high-dimensional thermal history in directed energy deposition processes via recurrent neural networks. *Manuf Lett* 18:35–39. <https://doi.org/10.1016/j.mfglet.2018.10.002>
 33. Farias FWC, da Cruz Payão Filho J, Moraes e Oliveira VHP (2021) Prediction of the interpass temperature of a wire arc additive manufactured wall: FEM simulations and artificial neural network. *Addit Manuf* 48:102387. <https://doi.org/10.1016/j.addma.2021.102387>
 34. Chen BQ, Hashemzadeh M, Guedes Soares C (2014) Numerical and experimental studies on temperature and distortion patterns in butt-welded plates. *Int J Adv Manuf Technol* 72:1121–1131. <https://doi.org/10.1007/s00170-014-5740-8>
 35. Bui MC, Le VT, Ta DX et al (2022) Thermal analysis in wire arc additively manufactured SS308L walls via numerical simulations. In: Long BT, Kim HS, Ishizaki K, Toan ND, Parinov IA, Kim YH (eds) *Proceedings of the International Conference on Advanced Mechanical Engineering, Automation, and Sustainable Development 2021 (AMAS2021)*. AMAS 2021. Lecture Notes in Mechanical Engineering, Springer, Cham. https://doi.org/10.1007/978-3-030-99666-6_2
 36. Goldak J, Chakravarti A, Bibby M (1984) A new finite element model for welding heat sources. *Metall Trans B* 15:299–305. <https://doi.org/10.1007/BF02667333>
 37. Lee SH (2020) CMT-based wire arc additive manufacturing using 316L stainless steel: effect of heat accumulation on the multi-layer deposits. *Metals* 10:278. <https://doi.org/10.3390/met10020278>
 38. Jurić I, Garašić I, Bušić M, Kožuh Z (2019) Influence of shielding gas composition on structure and mechanical properties of wire and arc additive manufactured Inconel 625. *Jom* 71:703–708. <https://doi.org/10.1007/s11837-018-3151-2>
 39. Dirisu P, Ganguly S, Mehmanparast A et al (2019) Analysis of fracture toughness properties of wire + arc additive manufactured high strength low alloy structural steel components. *Mater Sci Eng A* 765:138285. <https://doi.org/10.1016/j.msea.2019.138285>
 40. Pham TQD, Hoang TV, Van Tran X et al (2022) Fast and accurate prediction of temperature evolutions in additive manufacturing process using deep learning. *J Intell Manuf*. <https://doi.org/10.1007/s10845-021-01896-8>

Publisher's Note Springer Nature remains neutral with regard to jurisdictional claims in published maps and institutional affiliations.

Springer Nature or its licensor (e.g. a society or other partner) holds exclusive rights to this article under a publishing agreement with the author(s) or other rightsholder(s); author self-archiving of the accepted manuscript version of this article is solely governed by the terms of such publishing agreement and applicable law.